DOI: 10.3901/CJME.2015.0907.109, available online at www.springerlink.com; www.cjmenet.com

Multi-objective Optimal Design of High Frequency Probe for Scanning Ion Conductance Microscopy

GUO Renfei[1], ZHUANG Jian[1, *], MA Li[2, 3], LI Fei[2, 3], and YU Dehong[1]

1 *School of Mechanical Engineering, Xi'an Jiaotong University, Xi'an 710049, China*
2 *School of Science, Xi'an Jiaotong University, Xi'an 710049, China*
3 *Bioinspired Engineering and Biomechanics Center(BEBC), Xi'an Jiaotong University, Xi'an 710049, China*

Received June 23, 2015; revised August 27, 2015; accepted September 7, 2015

Abstract: Scanning ion conductance microscopy(SICM) is an emerging non-destructive surface topography characterization apparatus with nanoscale resolution. However, the low regulating frequency of probe in most existing modulated current based SICM systems increases the system noise, and has difficulty in imaging sample surface with steep height changes. In order to enable SICM to have the capability of imaging surfaces with steep height changes, a novel probe that can be used in the modulated current based hopping mode is designed. The design relies on two piezoelectric ceramics with different travels to separate position adjustment and probe frequency regulation in the *Z* direction. To further improve the resonant frequency of the probe, the material and the key dimensions for each component of the probe are optimized based on the multi-objective optimization method and the finite element analysis. The optimal design has a resonant frequency of above 10 kHz. To validate the rationality of the designed probe, microstructured grating samples are imaged using the homebuilt modulated current based SICM system. The experimental results indicate that the designed high frequency probe can effectively reduce the spike noise by 26% in the average number of spike noise. The proposed design provides a feasible solution for improving the imaging quality of the existing SICM systems which normally use ordinary probes with relatively low regulating frequency.

Keywords: scanning ion conductance microscopy(SICM), multi-objective optimization, high frequency probe, finite element analysis, imaging quality

1 Introduction

Scanning ion conductance microscopy(SICM), first presented by HANSMA, et al[1], is one kind of non-contact surface topography characterization techniques with high resolution(micrometer to nanometer scale). Compared with atomic force microscopy(AFM)[2] using a "contact" or "tapping" scanning mode, SICM can avoid deforming or damaging the sample surface during measuring process for its "non-contact" scanning mode[3]. And compared with scanning electron microscopy(SEM)[4], SICM does not require complex sample pretreatment steps, such as dehydrating, fixing, and metal spraying, thus making SICM suitable to *in situ* measure the topological and mechanical properties of various samples.

However, there are still some challenges in the present SICM measuring system. One challenge is how to improve the imaging quality, meanwhile maintain the ability of imaging complex sample surfaces with abrupt topography changes. Previous efforts attempted to address this issue mainly by varying the scanning modes. The scanning modes of SICM are mainly classified into two types according to the feedback signal type. One type directly uses the ion current as the feedback signal, such as the DC mode[5]. The other type uses the modulated current as the feedback signal, such as the AC mode presented by SHEVCHUK, et al[6], PASTRE, et al[7], and LI, et al[8], respectively. Since the DC mode cannot overcome the DC drift, which has great effect on the imaging quality, it cannot truly reflect the surface topography of the sample. In addition, DC mode can only characterize samples with very flat surfaces. The samples with rough surfaces would cause the SICM probe breaking and even breakdown of the feedback control[9]. The AC mode can effectively overcome the DC drift and contribute to obtaining more smooth measuring results with more detailed features. However, most existing modulated current based SICM systems use only one piezoelectric ceramic to simultaneously perform the frequency regulation and position adjustment of the probe, resulting in a low probe regulating frequency(normally$<$2 kHz), and therefore limiting the number of acquired sample data in unit time and decreasing the robustness of the SICM system to noise. Consequently,

* Corresponding author. E-mail: zhuangjian@mail.xjtu.edu.cn
Supported by National Natural Science Foundation of China(Grant No. 51375363)

low probe regulating frequency could increase the probability of reading sample data into error, and bring about extra noise during measuring process. Moreover, AC mode cannot image surfaces with abrupt changes in height, either. Although the hopping mode presented by NOVAK, et al[9](or named as backstep or standing approach mode[10–11] of SICM) can image any complex surfaces with steep changes in height, it has a lower probe regulating frequency due to its larger hopping distance. And since the hopping mode also uses the direct ion current as the feedback signal, it also suffers from the problem of slow DC drift, thus influences the SICM imaging quality[12]. Therefore, although SICM has been used in various applications in recent five years[13–22], further researches are still needed to deal with the challenges mentioned above.

In this manuscript, a high frequency SICM probe used in the modulated current based hopping mode is designed by combining the multi-objective optimization method with the finite element analysis. The design in this work not only holds the advantages of overcoming the DC drift of AC mode and imaging surface with steep changes in height of the hopping mode, but also improves the regulating frequency of the probe. Therefore, it could reduce the possibility of reading sample data in error of the SICM system, which may contribute to reducing the system noise. And the imaging experimental results of grating structures indicate that the high frequency probe designed in our work can effectively reduce the number of spike noise, thus improving the imaging quality of the existing SICM systems.

2 Multi-objective Optimal Design of the High Frequency SICM Probe

2.1 Structure and optimization parameters

The basic structure of the designed high frequency SICM probe is shown in Fig. 1. A quarter of the assembly is cut away around the axis of nanopipette for better explanation. Different from the existing modulated current based SICM systems with using only one piezoelectric ceramic, our design used two piezoelectric ceramics to separate probe frequency regulation and position adjustment in the Z direction. The annular piezoelectric ceramic with short travel was placed inside the high frequency probe, and was used to generate high frequency vibration. And then the resulting modulated ion current signal was used as the feedback signal. The other piezoelectric ceramic with long travel was used to modulate the position of the high frequency probe in Z-direction to perform imaging complex sample surfaces. This design makes probe frequency regulation free from the constraint of hopping distance, and thus could improve the imaging quality.

Besides using piezoelectric ceramic with high resonant frequency, the material and dimensional parameters should also be optimized to improve probe regulating frequency. The overall size and the total mass of the probe are limited by the boundary dimensions of the commercial products(i.e., piezoelectric ceramic, nanopipette). If a higher resonant frequency is required, the overall stiffness of the probe needs to be improved, which could increase the total mass of the probe. In order to get a balance between improving the resonant frequency and increasing the total mass, the multi-objective optimization algorithm and the finite element simulations are combined to realize the material selection and optimizations of the key dimensions for each component of the probe.

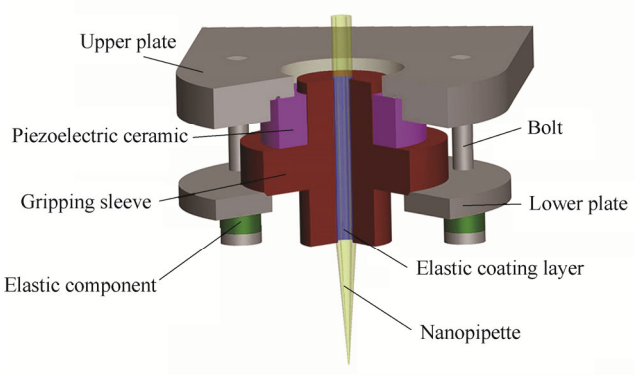

Fig. 1. Scheme of the designed SICM high frequency probe

The multi-objective optimization for determining the materials and the key dimensions of probe components can be defined as Eqs. (1)–(3) from the minimization point of view:

$$\min\ F(\boldsymbol{X})=\left(\frac{1}{f(\boldsymbol{X})},m(\boldsymbol{X})\right), \tag{1}$$

$$\boldsymbol{X}=\left(\boldsymbol{x}_1,\boldsymbol{x}_2,\boldsymbol{x}_3,\boldsymbol{x}_4,\boldsymbol{x}_5,\boldsymbol{x}_6\right)^{\mathrm{T}}, \tag{2}$$

$$\boldsymbol{x}_i=\left(\boldsymbol{u}_i,\boldsymbol{v}_i\right)\subseteq\mathbf{S}\subseteq\mathbf{R}^{\mathbf{n}}. \tag{3}$$

Where $F(\boldsymbol{X})$ is the two-dimensional vector of objective functions, $f(\boldsymbol{X})$ and $m(\boldsymbol{X})$ denote the resonant frequency function and the total mass function of the probe respectively; $\boldsymbol{X}$ is the decision vector, each element of which corresponds to one component of the probe. That is, $\boldsymbol{x}_1$ to $\boldsymbol{x}_6$ stand for gripping sleeve, nanopipette, lower plate, elastic component, bolt, and upper plate, respectively. $\boldsymbol{u}_i$ and $\boldsymbol{v}_i$ denote the material and dimension parameter vectors of component $\boldsymbol{x}_i$ respectively; $\mathbf{S}$ represents the feasible region of the decision vector; $\mathbf{R}^{\mathbf{n}}$ is the n-dimensional real number space.

2.1.1 Key dimensional parameters

The key dimensions in probe design mainly include the shape dimensions and the location dimensions used for assembling. The shape dimensions directly affect the total mass and the resonant frequency of the probe. The location dimension has great influence on the working state of the probe. Key dimensional parameters for each component of

the designed probe are shown in Fig. 2. The value range of the parameters for each probe component is not only limited by the dimensions of the commercial products, but also by the constraints illustrated in Table 1, which can avoid the interference among the assembly parts.

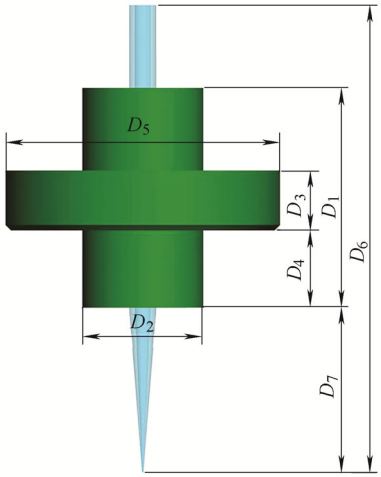

(a) Gripping sleeve and nanopipette

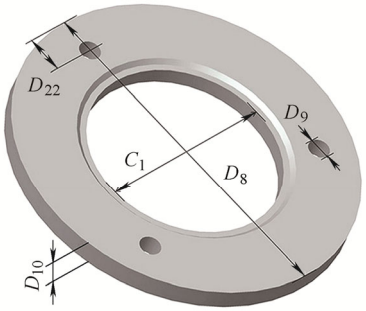

(b) Lower plate

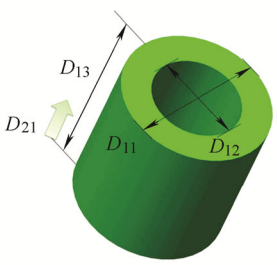

(c) Elastic component

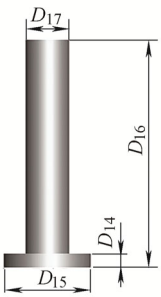

(d) Bolt

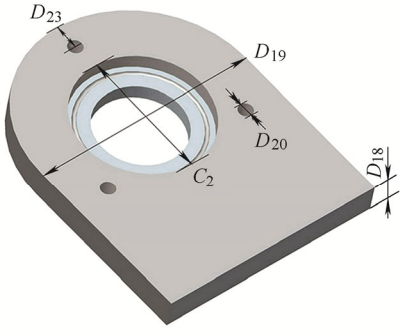

(e) Upper plate

Fig. 2. Schemes of the key dimensions for each component of the SICM probe

Table 1. Dimensional parameters and constraints for each component of the SICM probe

Dimensional parameter	Description	Value range V_r/mm	Constraint
D_1	Length	5–11	
D_2	Diameter	3–4.4	
D_3	Flange thickness	1–4	$C_1<D_5<(D_8+C_1-2\times D_{17})/2$
D_4	Flange position	1–5	$0<D_1-D_4-D_3$
D_5	Flange diameter	9.2–11.2	$D_5>D_2$
D_6	Length	10–18	
D_7	Position	4–9	$D_7<D_6$
D_8	Outer diameter	13.2–16	$D_8=D_{19}$
D_9	Hole diameter		$D_9=1.1\times D_{17}$
D_{10}	Thickness	0.6–1.8	
D_{11}	Outer diameter	1.7–2.4	$D_{11}=D_{15}$
D_{12}	Inner diameter	1–1.8	$D_{12}=D_{17}$
D_{13}	Height	0.8–2	
D_{14}	End height	0.55–2.05	
D_{15}	End diameter	1.7–2.4	
D_{16}	Length		$D_{14}+D_{13}+D_{10}+D_3+2.45+D_{18}/2=D_{16}$
D_{17}	Diameter	1–1.8	$D_{17}=D_{12}=D_{20}$
D_{18}	Thickness	1–2	
D_{19}	Outer diameter	13.2–16	$D_{19}=D_8$
D_{20}	Hole diameter	1–1.8	$D_{20}=D_{17}$
D_{21}	Pre-compression	0–0.2	
D_{22}	Hole position		$D_{22}=(D_8-C_1)/4$
D_{23}	Hole position		$D_{23}=D_{22}$
C_1	Inner diameter	9	
C_2	Inner diameter	9	$C_1=C_2$

2.1.2 *Material parameters*

In all the components of the high frequency probe, the materials of nanopipette(Borosilicate glass, BF100-58-10, Sutter Instrument) and the piezoelectric ceramic(PIC 255, PI, Germany) are definitive. Therefore, only five components(i.e., the gripping sleeve, the lower plate, the elastic component, the bolts and the upper plate) need optimization. In this study, seven materials, such as rubber, two kinds of nylon materials, polymethylmethacrylate (PMMA), aluminum alloy, beryllium bronze(QBe2) and stainless steel had been used. The properties of each material used for optimizations are shown in Table 2.

Table 2. Materials and corresponding properties used for optimizations

Material	Young modulus E/MPa	Density ρ/(kg • m^{-3})	Poisson ratio γ
Rubber	7.84	1200	0.47
Nylon 01	1070	1040	0.34
Nylon 02	2830	1100	0.4
PMMA	3800	1180	0.4
Aluminum alloy	71 000	2770	0.33
QBe2	125 000	8250	0.3
Stainless steel	200 000	7850	0.3
Borosilicate glass	76 000	2235	0.23
PIC255*	$E_1=E_2=62\ 100$	7800	$\gamma_{13}=\gamma_{23}=0.44$
	$E_3=48\ 300$		$\gamma_{12}=0.32$

* Note: E_1 /E_2 /E_3 and $\gamma_{13}/\gamma_{23}/\gamma_{12}$ denote the Young modulus and the Poisson ratio of the piezoelectric ceramic in the direction of X, Y, and Z, respectively[23].

2.2 Multi-objective optimal design of the probe

To achieve the multi-objective optimizations of the materials and the key dimensions of probe, the improved NSGA-II algorithm[24] combined with the ANSYS 15.0 software(ANSYS Inc., Canonsburg, PA) was applied. Compared to the standard NSGA-II algorithm, the improved algorithm can handle sample data with features of higher dimensions and remove the unreasonable solutions. The object function of the multi-objective optimization is to maximize the resonant frequency and minimize the total mass of the probe. Because the total mass and the resonant frequency of the probe can be obtained directly from the finite element simulations, the specific expression of the objective function is not needed in this work. One object generally generates resonance near the natural frequency, and the first order natural frequency determines the limitation of the working frequency of the probe. Hence, the first order natural frequency is regarded as the resonant frequency herein. By applying static structural analysis and prestressed modal analysis to the geometric model of the probe, the values of the objective functions can be obtained. Considering the drive capability of the piezoelectric ceramic, the feasible solution minimizing the total mass of the probe was chosen as the optimal solution when the variation δ of the resonant frequency was not significant($|\delta|<2\%$).

2.2.1 Encoding mode

In this work, the real number encoding was adopted to encode the material and dimension parameters of the probe, and the specific encoding mode is described as follows. $\{u_{11},\cdots, u_{17}, v_{11},\cdots, v_{15}, u_{21},\cdots, u_{27}, v_{21}, v_{22}, u_{31},\cdots, u_{37}, v_{31}, \cdots, v_{35}, u_{41},\cdots, u_{47}, v_{41},\cdots, v_{44}, u_{51},\cdots, u_{57}, v_{51},\cdots, v_{54}, u_{61}, \cdots, u_{67}, v_{61},\cdots, v_{65}\}$, where u_{i1}–$u_{i7}(i = 1, 2,\cdots, 7)$ denote the seven candidate materials of the i-th component in turn, assignment of 1 indicates the selected corresponding material, and assignment of 0 indicates the corresponding material which is not selected. v_{ij} denotes the value of the j-th dimension parameter for the i-th component. All the dimension parameters should satisfy the constraints listed in Table 1.

2.2.2 Multi-objective optimization procedure

Multi-objective optimization procedure of determining the materials and the key dimensions of the probe is described as follows.

(1) Generate randomly n decision vectors of the probe that satisfy the constraints listed in Table 1, i.e., the parent population $\boldsymbol{P}$. And the ANSYS software is called to compute the values of the objective functions for each decision vector, including the resonant frequency and the total mass of the probe. Then the maximum number of generations I, the probability of selection p_1, the probability of crossover p_2, and the probability of mutation p_3 are set.

(2) Obtain the child population $\boldsymbol{Q}$ by operations of selection, crossover, and mutation on the parent population $\boldsymbol{P}$. The values of each individual in $\boldsymbol{Q}$ are delivered to the geometric model in ANSYS to update the material and dimension parameters of the probe. Then ANSYS is called to compute the values of the objective functions for each decision vector.

(3) Sort the individuals in the population $\boldsymbol{T}=\boldsymbol{P}\cup\boldsymbol{Q}$ according to the values of the objective functions, retain and archive the first n feasible solutions, and then update the parent population $\boldsymbol{P}$.

(4) Check the number of generations t. If $t<I$, jump to step (2), otherwise sort the archived feasible solutions. The feasible solution minimizing the total mass of the probe is chosen as the optimal design parameters if the variation δ of the resonant frequency is not significant($|\delta|<2\%$).

The parameters used for multi-objective optimization and simulations are listed below. The size of the parent population $\boldsymbol{P}$ is n=10, the probability of selection p_1=0.5, the probability of crossover p_2=0.7, the probability of mutation p_3=0.05, and the maximum number of generations I=50. Based on these conditions, the optimal materials and dimension parameters for each component of the high frequency probe are shown in Table 3.

Table 3. Optimal design parameters of the probe

Component	Optimal material	Dimension parameter	Description	Optimal value O_v/mm
Gripping sleeve	Nylon01	D_1	Length	6.0
		D_2	Diameter	4.4
		D_3	Flange thickness	1.5
		D_4	Flange position	3.0
		D_5	Flange diameter	10
Nanopipette	Borosilicate glass	D_6	Length	13
		D_7	Position	6.0
		D_8	Outer diameter	13.2
Lower plate	Aluminum alloy	D_9	Hole diameter	1.1
		D_{10}	Thickness	0.7
		C_1	Inner diameter	9.0
		D_{22}	Hole position	1.05
Elastic component	Nylon01	D_{11}	Outer diameter	1.7
		D_{12}	Inner diameter	1.0
		D_{13}	Height	0.8
		D_{21}	Pre-compression	0
Bolt	Aluminum alloy	D_{14}	End height	0.55
		D_{15}	End diameter	1.7
		D_{16}	Length	6.5
Upper plate	Aluminum alloy	D_{17}	Diameter	1.0
		D_{18}	Thickness	1.0
		D_{19}	Outer diameter	13.2
		D_{20}	Hole diameter	1.0
		C_2	Inner diameter	9.0
		D_{23}	Hole position	1.05
Piezoelectric ceramic	PIC255	–	–	–

The probe with the above optimal design parameters has a resonant frequency of 20.473 kHz and a total mass of 1.535 g. This resonant frequency is far higher than the existing probe(less than 2 kHz). Note that the minimization of the total mass was preferred in the above optimizations.

Higher resonant frequency would be available at the cost of increasing the total mass. The photograph of the designed high frequency probe is shown in Fig. 3.

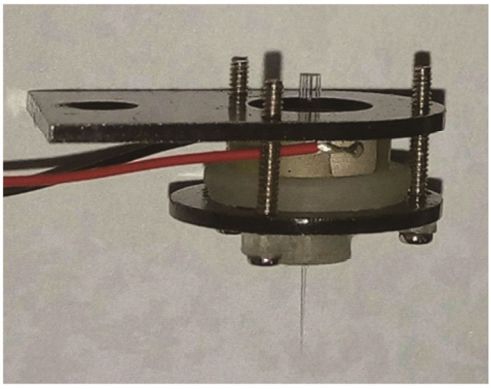

Fig. 3. Photograph of the fabricated high frequency probe

3 Experiments and Discussion

3.1 Modulated current based SICM system

Fig. 4 shows the SICM system with the high frequency probe. The system composition is described in details as follows. The coarse positions of the probe in three directions are provided by the DC motors(M111.1 DG, PI, Germany) with 15 mm stroke. The XY piezoelectric ceramic(P621.2CL, PI, Germany) is mounted to the XY motors for precision positioning of the probe in XY direction. The Z-direction piezoelectric ceramic with 100 μm stroke(P621.ZCL, PI, Germany) is mounted to the XY piezoelectric ceramic for precision positioning of the probe in Z direction. The designed high frequency probe(HF Probe in Fig. 4(b)) is mounted to the Z motor. The annular piezoelectric ceramic(PD080.30, PI, Germany) inside the probe, which has a 2 μm stroke and an axial resonant frequency of 500 kHz, is used to drive the probe to generate a high frequency vibration.

The modulated current based hopping mode is the same as the conventional hopping mode except that the rate of change in ion current is used as the feedback signal. Driven by the high frequency sinusoidal signal generated by the FPGA controller, the high frequency probe could generate high frequency vibration. The resulting modulated ion current is then amplified with a current preamplifier and synchronously sampled by the AD module of the FPGA controller at a frequency of 200 kHz. The DA module of the FPGA controller outputs the control signal based on the rate of change in ion current. The control signals are then amplified by the low voltage PZT amplifier(E-503, PI, Germany) to drive the piezoelectric ceramics to move in the three directions and closed-loop controlled by the position servo-control module(E-509, PI, Germany).

3.2 Frequency spectrum of the high frequency probe

According to the imaging principle of SICM, the ion voltage converted from the ion current by a current preamplifier changes in the same discipline as the position of the probe changes in the working space. Therefore, the change of ion voltage at different drive frequencies can reflect the vibration characteristics of the probe tip. The specific test method used in experiments is described as follows.

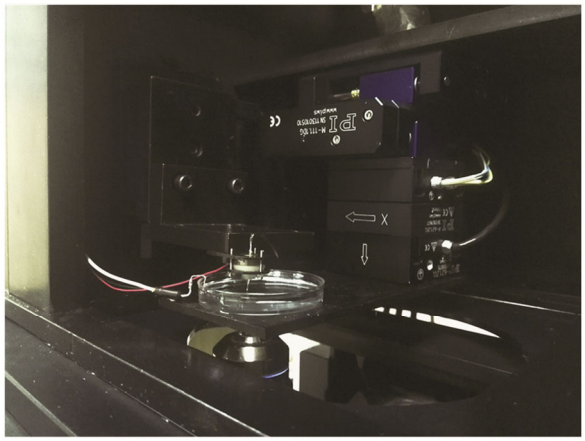

(a)

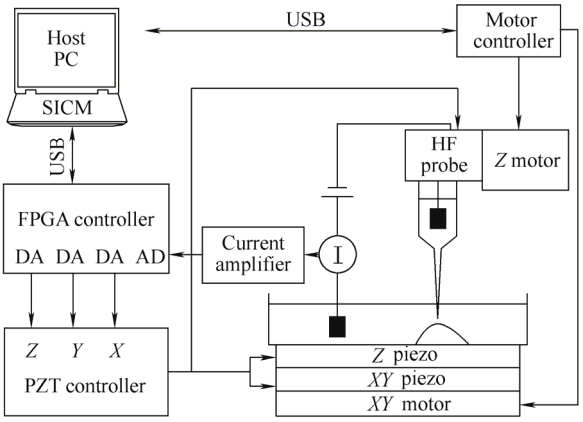

(b)

Fig. 4. Photograph and the scheme of the SICM system

(1) Adjust the piezoelectric ceramic with long stroke in the Z direction to make the distance between the probe tip and the bottom surface of the petri dish approximately equal to the inner tip radius of the probe. The probe tip is then in the working space.

(2) Apply sinusoidal drive signals to the annular piezoelectric ceramic of the high frequency probe. The drive frequencies range from 200 Hz to 20.2 kHz, and the frequency increment is 200 Hz.

(3) Obtain the decrease ΔV of ion voltage at stable state by sampling and recording the ion voltage signals with the AD module of the SICM system.

(4) The relationship between the drive frequency and the decrease ΔV of ion voltage could reflect the frequency spectrum of the probe.

Fig. 5 shows the test result of the probe frequency spectrum. The resonant frequency of the high frequency probe is about 15.6 kHz, which is lower than the simulation result of 20.5 kHz by 23.8%. This may be due to the dimension errors of machining, the dimension fluctuations of the pulled nanopipettes, or the positioning errors of assembly. All of these could cause mismatch between the

simulation data and the actual data. The uncertainty of tip topography of the pulled nanopipette can be diminished by polishing the surface of the nanopipette tip[25–26], decorating the tip geometry with coating material[27], or estimating the tip geometry with systematic experiments[28]. The obtained detailed geometry information can help to reduce the difference between the simulation data and the actual tip geometry. Because the implementations of these methods require specialized equipment, such as polishing machine, chemical vapor deposition(CVD) apparatus, etc., which are beyond the scope of this research, so there is no more detailed discussion here. But the test result is still much better than the existing probes, and is adequate for the subsequent SICM imaging experiments.

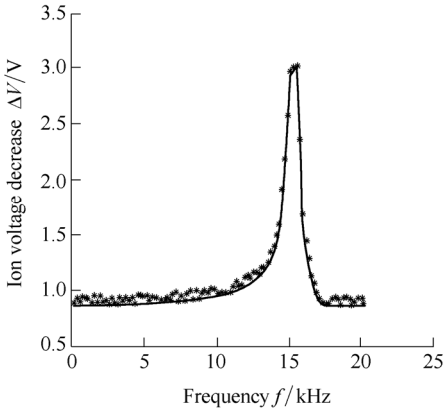

Fig. 5. Frequency spectrum of the high frequency probe

3.3 Verification of the imaging quality

In order to verify the efficiency of the designed high frequency probe, the grating structures fabricated by lithography technique[29] were imaged using the modulated current based SICM system with the designed high frequency probe. The cycle of the grating and the height of sample are about 6 μm and 0.6 μm, respectively. The sample in the petri dish was covered with 0.1 M KCl aqueous solution.

Fig. 6(a) is the optical image of the grating sample. Fig. 6(b) and Fig. 6(c) are the corresponding SICM imaging results. It can be observed that the juncture between two grating structures(shown as ambiguous dark stripes in Fig. 6(a) with width larger than 2 μm) is apparently larger than that imaged by SICM in Fig. 6(b), although the visual appearances of the two microscopies are overall consistent. This is mainly due to that the resolution of ordinary optical microscopy can hardly exceed 200 nm due to the limitation of the optical diffraction limit. While SICM, as one kind of scanning probe microscopy whose resolution is only dependent on the inner diameter of the probe tip, can obtain image with higher resolution and better accuracy when using probe with smaller tip diameter. As observed in Fig. 6 (c), the sample is not placed horizontally and thus is hard to get accurate optical image. But the angle between the sample and the horizontal plane can be obtained by simply analyzing the 3D SICM data(about 7.6° in Fig. 6(c)). It indicates that SICM can obtain accurate 3D topographical information with high resolution, which is one of the most important advantages of SICM compared to the optical microscopy. This is of great importance for experimental situations where accurate positioning is needed, such as researches about the toxic action of drugs on specified cell structure[30–33], and the delivery of small biological particles to specified living cells[22, 34–36].

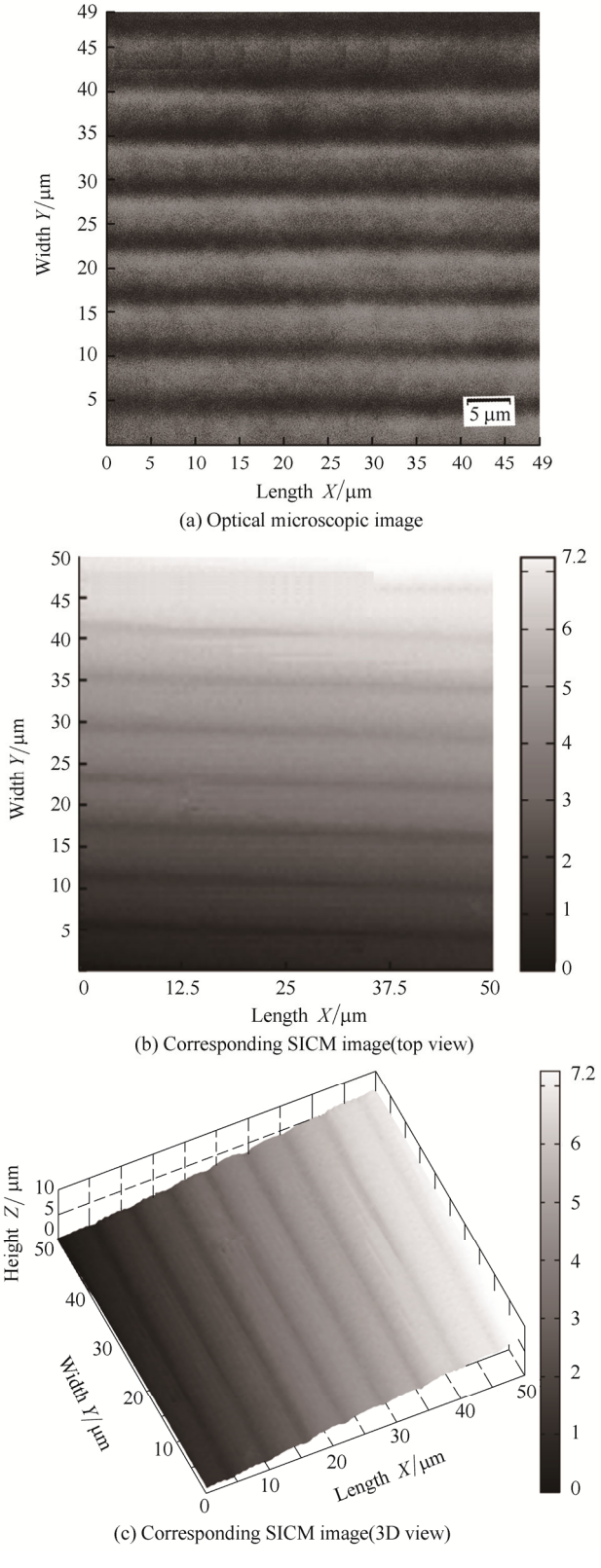

Fig. 6. Comparison of imaging results of the grating sample

To further investigate the influence of the designed high frequency probe on the imaging quality, the same sample area was imaged by the ordinary probe and the high frequency probe in turn. The imaging parameters were the same: the imaging size was set to 200×200 pixels, the step size in horizontal direction(*XY*) was 100 nm, and the hopping distance in *Z* direction was set to 5 μm. The imaging results for comparison are shown in Fig. 7.

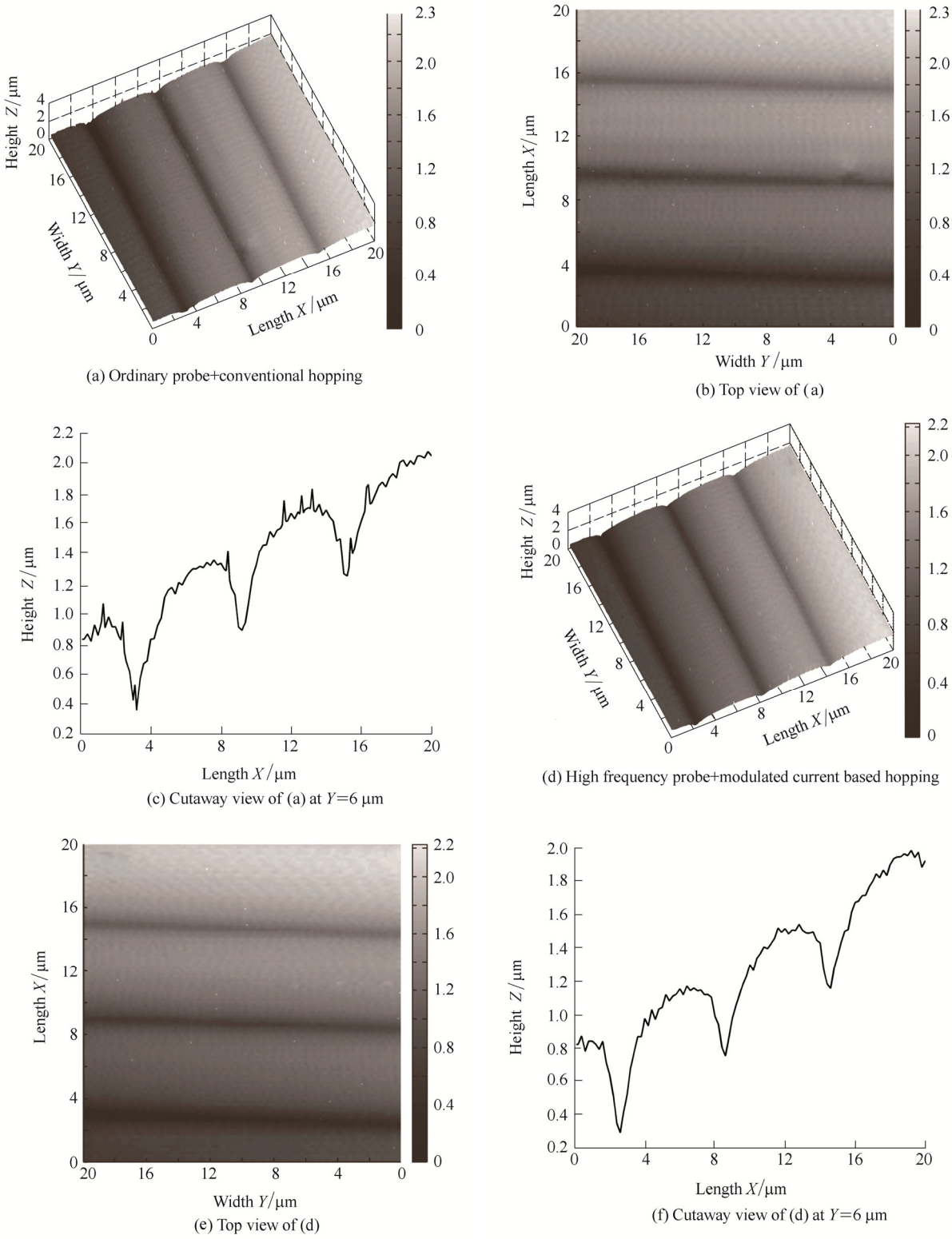

Fig. 7. Comparison of SICM imaging results using two different probes

Figs. 7(a)–(c) are the SICM imaging results using the ordinary probe and the conventional hopping mode. Fig. 7(a) is the 3D view, Fig. 7(b) is the top view and Fig. 7(c) is the cutaway view at *Y*=6 μm. It can be observed that the outline of each grating structure is quite apparent, and the distance between two gratings is uniform(6.0±0.05 μm). But there is noticeable noise appearing as spikes in Fig. 7(c). Figs. 7(d)–(f) display images obtained using the high

frequency probe and the modulated current based hopping mode. Fig. 7(d) is the 3D view, Fig. 7(e) is the top view and Fig. 7(f) is the cutaway view at Y=6 μm. The imaging result agrees well with that of using the ordinary probe. But as seen from the profile data in Fig. 7(f), the imaging results using the high frequency probe and the modulated current based hopping mode have less spike noise.

The same sample area was imaged for 50 times using the above two probes in turn. The number of spikes in each scan was recorded for statistical analysis. Because the sample surface is relatively smooth while the spike noise has a steep increase and decrease in height, the number of spike noise can be simply calculated by detecting the height variations of adjacent pixels in sampling section. A spike noise is detected if the difference between the pixel height and the average height of the sampling section is bigger than a predefined threshold(i.e., 0.07 μm herein).The results are shown in Fig. 8. In Fig. 8(b) of the box plot of one-way analysis of variance(ANOVA), the type of probe shows to have significant effect on the number of spikes($p<0.001$), and the number of spikes using the high frequency probe is generally fewer than that using the ordinary probe. The average number of spike noise decreases by 26%(from 34 to 25) with using the designed probe. This is reasonable because the improvement of the regulating frequency of the probe can help the system to obtain more sample data within the same period of time. More sample data could contribute to enhancing the robustness of the system to various noise signals and reducing the number of sample data that read in error. Thus, the high frequency probe is proven to be helpful for improving the SICM imaging quality.

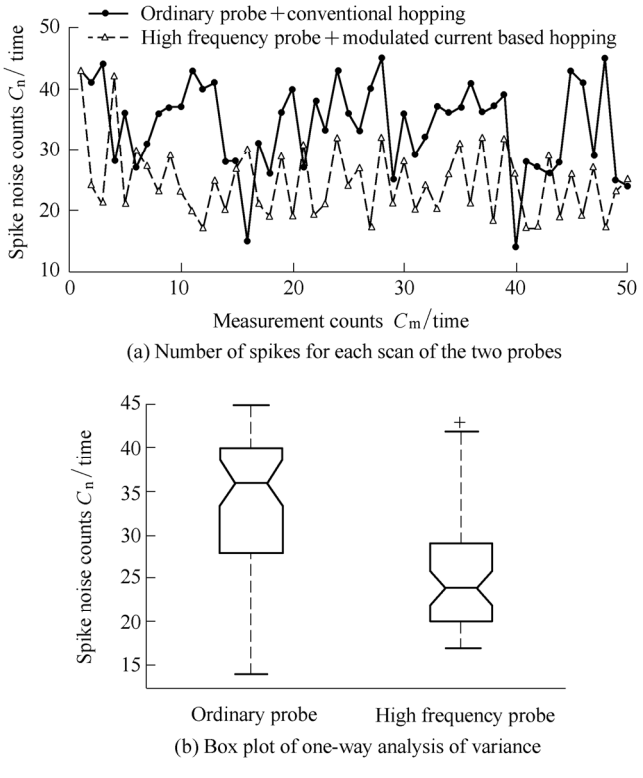

Fig. 8. Statistical analysis of the spike noise

4 Conclusions

(1) A novel high frequency probe with the advantages of overcoming the DC drift problem and capability of imaging surface with abrupt height changes is designed for the SICM system.

(2) High regulating frequency of above 10 kHz is achieved by combining the multi-objective optimization algorithm with the finite element analysis to optimize the material parameters and the dimensional parameters.

(3) The designed high frequency probe contributes to reducing the number of spike noise of the SICM system when the modulated current based hopping mode is applied.

(4) The experimental results prove the rationality of our design and provide a feasible solution for improving the imaging quality of existing SICM systems which use an ordinary probe with lower regulating frequency.

References

[1] HANSMA P K, DRAKE B, MARTI O, et al. The scanning ion-conductance microscope[J]. *Science*, 1989, 243(4891): 641–643.

[2] ANDO T. High-speed AFM imaging[J]. *Current Opinion in Structural Biology*, 2014, 28: 63–68.

[3] USHIKI T, NAKAJIMA M, CHOI M, et al. Scanning ion conductance microscopy for imaging biological samples in liquid: a comparative study with atomic force microscopy and scanning electron microscopy[J]. *Micron*, 2012, 43(12): 1390–1398.

[4] SOKOLOVA V, LUDWIG A, HORNUNG S, et al. Characterisation of exosomes derived from human cells by nanoparticle tracking analysis and scanning electron microscopy[J]. *Colloids and Surfaces B: Biointerfaces*, 2011, 87(1): 146–150.

[5] KORCHEV Y E, MILOVANOVIC M, BASHFORD C L, et al. Specialized scanning ion-conductance microscope for imaging of living cells[J]. *Journal of Microscopy*, 1997, 188(1): 17–23.

[6] SHEVCHUK A I, GORELIK J, HARDING S E, et al. Simultaneous measurement of Ca2+ and cellular dynamics: combined scanning ion conductance and optical microscopy to study contracting cardiac myocytes[J]. *Biophysical Journal*, 2001, 81(3): 1759–1764.

[7] PASTRE D, IWAMOTO H, LIU J, et al. Characterization of AC mode scanning ion-conductance microscopy[J]. *Ultramicroscopy*, 2001, 90(1): 13–19.

[8] LI C, JOHNSON N, OSTANIN V, et al. High resolution imaging using scanning ion conductance microscopy with improved distance feedback control[J]. *Progress in Natural Science*, 2008, 18(6): 671–677.

[9] NOVAK P, LI C, SHEVCHUK A I, et al. Nanoscale live-cell imaging using hopping probe ion conductance microscopy[J]. *Nature Methods*, 2009, 6(4): 279–281.

[10] HAPPEL P, DIETZEL I D. Backstep scanning ion conductance microscopy as a tool for long term investigation of single living cells[J]. *Journal of Nanobiotechnology*, 2009, 7(7): 7.

[11] TAKAHASHI Y, MURAKAMI Y, NAGAMINE K, et al. Topographic imaging of convoluted surface of live cells by scanning ion conductance microscopy in a standing approach mode[J]. *Physical Chemistry Chemical Physics*, 2010, 12(34): 10012–10017.

[12] HAPPEL P, THATENHORST D, DIETZEL I D. Scanning ion conductance microscopy for studying biological samples[J]. *Sensors*, 2012, 12(11): 14 983–15 008.

[13] LIPSON A L, GINDER R S, HERSAM M C. Nanoscale in situ characterization of Li-ion battery electrochemistry via scanning ion conductance microscopy[J]. *Advanced Materials*, 2011, 23(47): 5613–5617.
[14] CHEN C, ZHOU Y, BAKER L A. Single nanopore investigations with ion conductance microscopy[J]. *ACS Nano*, 2011, 5(10): 8404–8411.
[15] LIU S, LI Q, SHAO Y. Electrochemistry at micro- and nanoscopic liquid/liquid interfaces[J]. *Chemical Society Reviews*, 2011, 40(5): 2236–2253.
[16] KLENERMAN D, SHEVCHUK A, NOVAK P, et al. Imaging the cell surface and its organization down to the level of single molecules[J]. *Philosophical Transactions of the Royal Society B: Biological Sciences*, 2013, 368(1611): 20120027.
[17] RHEINLAENDER J, SCHAEFFER T E. Mapping the mechanical stiffness of live cells with the scanning ion conductance microscope[J]. *Soft Matter*, 2013, 9(12): 3230–3236.
[18] SCHAFFER T E. Nanomechanics of molecules and living cells with scanning ion conductance microscopy[J]. *Analytical Chemistry*, 2013, 85(15): 6988–6994.
[19] RHEINLAENDER J, VOGEL S, SEIFERT J, et al. Imaging the elastic modulus of human platelets during thrombin-induced activation using scanning ion conductance microscopy[J]. *Thromb Haemost*, 2015, 113(2): 305–311.
[20] MCKELVEY K, KINNEAR S L, PERRY D, et al. Surface charge mapping with a nanopipette[J]. *Journal of the American Chemical Society*, 2014, 136(39): 13735–13744.
[21] NASHIMOTO Y, TAKAHASHI Y, IDA H, et al. Nanoscale imaging of an unlabeled secretory protein in living cells using scanning ion conductance microscopy[J]. *Analytical Chemistry*, 2015, 87(5): 2542–2545.
[22] IVANOV A P, ACTIS P, JÖNSSON P, et al. On-demand delivery of single DNA molecules using nanopipets[J]. *ACS Nano*, 2015, 9(4): 3587–3595.
[23] GHORBEL S. *Couplage électromécanique effectif dans les structures piézoélectriques expérimentations, simulations et corrélations*[D]. Châtenay-Malabry, Hauts-de-Seine: École Centrale Paris, 2009.
[24] XIA H, ZHUANG J, YU D. Novel soft subspace clustering with multi-objective evolutionary approach for high-dimensional data[J]. *Pattern Recognition*, 2013, 46(9): 2562–2575.
[25] ELSAMADISI P, WANG Y, VELMURUGAN J, et al. Polished nanopipets: new probes for high-resolution scanning electrochemical microscopy[J]. *Analytical Chemistry*, 2011, 83(3): 671–673.
[26] MALBOUBI M, GU Y, JIANG K. Surface properties of glass micropipettes and their effect on biological studies[J]. *Nanoscale Research Letters*, 2011, 6(1): 1–10.
[27] LIU S, DONG Y, ZHAO W, et al. Studies of ionic current rectification using polyethyleneimines coated glass nanopipettes[J]. *Analytical Chemistry*, 2012, 84(13): 5565–5573.
[28] CALDWELL M, DEL LINZ S J L, SMART T G, et al. Method for estimating the tip geometry of scanning ion conductance microscope pipets[J]. *Analytical Chemistry*, 2012, 84(21): 8980–8984.
[29] YE X, DING Y, DUAN Y, et al. Room-temperature capillary-imprint lithography for making micro-/nanostructures in large areas[J]. *Journal of Vacuum Science & Technology B*, 2010, 28(1): 138–142.
[30] YANG X, LIU X, LU H, et al. Real-time investigation of acute toxicity of ZnO nanoparticles on human lung epithelia with hopping probe ion conductance microscopy[J]. *Chemical Research in Toxicology*, 2012, 25(2): 297–304.
[31] LIN X, O'MALLEY H, CHEN C, et al. Scn1b deletion leads to increased tetrodotoxin-sensitive sodium current, altered intracellular calcium homeostasis and arrhythmias in murine hearts[J]. *The Journal of physiology*, 2015, 593(6): 1389–1407.
[32] NIKOLAEV V O, MOSHKOV A, LYON A R, et al. β_2-adrenergic receptor redistribution in heart failure changes cAMP compartmentation[J]. *Science*, 2010, 327(5973): 1653–1657.
[33] BHARGAVA A, LIN X, NOVAK P, et al. Super-resolution scanning patch clamp reveals clustering of functional ion channels in adult ventricular myocyte[J]. *Circulation Research*, 2013, 112(8): 1112–1120.
[34] BRUCKBAUER A, YING L, ROTHERY A M, et al. Writing with DNA and protein using a nanopipet for controlled delivery[J]. *Journal of the American Chemical Society*, 2002, 124(30): 8810–8811.
[35] BABAKINEJAD B, JONSSON P, LOPEZ C A, et al. Local delivery of molecules from a nanopipette for quantitative receptor mapping on live cells[J]. *Analytical Chemistry*, 2013, 85(19): 9333–9342.
[36] OZAWA T, ITO Y, NAGAI M, et al. Electrokinetic intracellular delivery combined with vibration-assisted cell membrane perforation[C]//*IEEE International Symposium on Micro-Nano Mechatronics and Human Science(MHS)*, Nagoya, Japan, November 10–13, 2013: 1–4.

Biographical notes

GUO Renfei, born in 1988, is currently a PhD candidate at *School of Mechanical Engineering, Xi'an Jiaotong University, China*. He received his bachelor degree from *Northwest A&F University, China,* in 2010. His research interests include optimal design and new applications of scanning ion conductance microscopy.
E-mail: guorenfei302088@stu.xjtu.edu.cn

ZHUANG Jian, born in 1974, received his B.Eng, MS and PhD degrees from *Xi'an Jiaotong University, China*, in 1996, 1999, and 2003, respectively. He is currently an associate professor at *School of Mechanical Engineering, Xi'an Jiaotong University, China*. His research is involved in micro/nano imaging technology, artificial intelligence, and electro-hydraulic control system.
E-mail: zhuangjian@mail.xjtu.edu.cn

MA Li, born in 1989, is currently a master candidate at *School of Science, Xi'an Jiaotong University, China*. She received her bachelor degree from *Xinyang Normal University, China*, in 2013. Her research interest is on the cell behavior using scanning ion conductance microscopy.
E-mail: mali890625@stu.xjtu.edu.cn

LI Fei, born in 1980, is currently an associate professor at *School of Science, Xi'an Jiaotong University, China.* She received her PhD degree from the *University of Warwick, United Kingdom*, in 2008. Her present research interests are on fabrications of high-resolution microscopic and nanoscopic probes and the application studies of novel scanning probe microscopy in biological field.
E-mail: feili@mail.xjtu.edu.cn

YU Dehong, born in 1949, joined *Xi'an Jiaotong University, China* in 1985, where he is currently a professor at *School of Mechanical Engineering, Xi'an Jiaotong University, China*. His research interests include mechanical design, plastic processing and electro-hydraulic control system.
E-mail: dhyu@mail.xjtu.edu.cn